



Full Electric Control of Exchange Bias at Room Temperature by Resistive Switching

Lujun Wei, Zhenzhong Hu, Guanxiang Du,* Yuan Yuan, Ji Wang, Hongqing Tu, Biao You, Shiming Zhou, Jiangtao Qu, Hongwei Liu, Rongkun Zheng, Yong Hu, and Jun Du*

Electric control of exchange bias (EB) is of vital importance in energy-efficient spintronics. Although many attempts have been made during the past decade, each has its own limitations for operation and thus falls short of full direct and reversible electrical control of EB at room temperature. Here, a novel approach is proposed by virtue of unipolar resistive switching to accomplish this task in a Si/SiO₂/Pt/Co/NiO/Pt device. By applying certain voltages, the device displays obvious EB in the high-resistance-state while negligible EB in the low-resistance state. Conductive filaments forming in the NiO layer and rupturing near the Co–NiO interface are considered to play dominant roles in determining the combined resistive switching and EB phenomena. This work paves a new way for designing multifunctional and nonvolatile magnetoelectric random access memory devices.

Spintronics which exploits both charge and spin degrees of freedom of electrons is considered to be a promising avenue for manufacturing new generation electronic devices.^[1,2] In particular, electric-field (E-field) controlled spintronics is of great importance in information technology as it aims at decreased electric power consumption, increased integration density, reversibility, nonvolatility, and increased data processing speed in comparison with conventional semiconductor devices.^[3,4] Since spintronic devices are generally made of multilayered thin-films, their performances depend strongly on the interface magnetism. Therefore, manipulating magnetism at thin-film interfaces, preferably by purely electrical means, sounds very intriguing for developing high-performance spintronic devices. However, the absence of direct coupling between magnetization

and electric field makes the electric control of surface and interface magnetism a scientific challenge. The significance of controlled interface magnetism started with the exchange bias (EB) effect, which is originated from exchange coupling between an antiferromagnet (AFM) and a ferromagnet (FM) when they are atomically adjacent to each other.^[5,6] Up to date, EB has been widely used in many applications, such as read heads and magnetic sensors, although the inherent mechanism has not been completely understood.^[6,7] Full control of EB with electric field allows for an additional degree of freedom in applications and provides a path to the full electrical control of magnetization.

Besides the potential applications, E-field control of EB could also offer a technique for exploring the EB mechanism.

To our knowledge, many studies of E-field control of EB were performed on magnetoelectric/magnetic heterostructures involving single phase magnetoelectric materials, such as Cr₂O₃,^[3,8,9] YMnO₃,^[10] and BiFeO₃,^[11–13] which are both ferroelectric/dielectric and antiferromagnetic below their Néel temperature. For examples, with Cr₂O₃ coupled to Pd-Co multilayers, He et al.^[3] claimed that it was possible to reversibly switch between two different EB polarity states at room temperature through the application of electric field and an additional applied magnetic field after magneto-electric field cooling. However, this effect can only be realized below the Néel

Dr. L. J. Wei, Dr. Y. Yuan, Dr. J. Wang, Dr. H. Q. Tu,
Prof. B. You, Prof. J. Du
National Laboratory of Solid State Microstructures
and Department of Physics
Nanjing University
Nanjing 210093, P. R. China
E-mail: jdu@nju.edu.cn

Z. Z. Hu, Prof. G. X. Du
College of Telecommunication and Information Engineering
Nanjing University of Posts and Telecommunications
Nanjing 210003, P. R. China
E-mail: duguanxiang@njupt.edu.cn

Prof. B. You, Prof. J. Du
Collaborative Innovation Center of Advanced Microstructures
Nanjing 210093, P. R. China

DOI: 10.1002/adma.201801885

Prof. S. M. Zhou
Department of Physics
Tongji University
Shanghai 200092, P. R. China

Dr. J. T. Qu, Prof. R. K. Zheng
School of Physics and the Australian Institute for
Nanoscale Science and Technology
The University of Sydney
NSW 2006, Australia

Dr. H. W. Liu
The Australian Centre for Microscopy and Microanalysis
The University of Sydney
NSW 2006, Australia

Prof. Y. Hu
College of Sciences
Northeastern University
Shenyang 110819, P. R. China

temperature of Cr_2O_3 ($T_N = 307 \text{ K}$ ^[3]). Wu et al.^[12] reported the creation of a multiferroic field effect device with a BiFeO_3 (antiferromagnetic-ferroelectric) gate dielectric and a $\text{La}_{0.7}\text{Sr}_{0.3}\text{MnO}_3$ (ferromagnetic) conducting channel that exhibits direct, full, and bipolar electrical control of EB. Although no field cooling, temperature cycling, or additional applied magnetic or electric field beyond the initial BiFeO_3 polarization is needed, this bipolar modulation effect can only be operated at quite a low temperature ($\approx 5.5 \text{ K}$).

On the other hand, the combination of AFM/FM exchange-biased systems and ferroelectric materials^[14,15] gives a new pathway to achieve reversible E-field-controlled magnetization reversal by combining strain-mediated magnetoelectric coupling and EB. Liu et al.^[14] realized a magnetization switching by nearly 180° at room temperature in $\text{FeMn}/\text{Ni}_{80}\text{Fe}_{20}/\text{FeGaB}/\text{PMN-PT}$ (lead zinc niobate-lead titanate) exchange-biased multiferroic system through E-field-tuned EB, however, this magnetization switching is irreversible. Chen et al.^[15] carefully investigated the angular dependence of E-field-controlled EB and magnetization reversal at room temperature in the exchange-biased $\text{Co}_{40}\text{Fe}_{40}\text{B}_{20}$ (CoFeB)/ $\text{Ir}_{25}\text{Mn}_{75}$ (IrMn) heterostructures deposited on a PMN-PT ferroelectric single crystal. They demonstrated that reversible electrical modulation of EB and magnetization reversal were obtained, which depend strongly on the angle between external magnetic field and the pinning direction. However, special angle and huge constant applied voltage ($\approx 400 \text{ V}$) are needed. Moreover, all these above strain-induced E-field control of EB are often volatile (i.e., not stable in the absence of an applied field), impeding the application in random access memory.

In this work, we report an alternative approach for E-field control of EB in the $\text{Si}/\text{SiO}_2/\text{Pt}/\text{Co}/\text{NiO}/\text{Pt}$ heterostructures by virtue of resistive switching (RS) effect in the NiO layer, which is reversible, nonvolatile, and able to be operated at room temperature as well. RS phenomenon refers to that reversible switching between a high-resistance state (HRS) and a low-resistance state (LRS) can be controlled by applying a certain voltage, which has been widely observed in various oxides when they are sandwiched by two metal electrodes.^[16–20] Resistive random access memory (RRAM) based on the RS effect has attracted a lot of interest in recent years because of its remarkable characteristics, such as low power consumption, high operation speed, nondestructive readout, etc.^[21] By applying appropriate voltages in the present $\text{Si}/\text{SiO}_2/\text{Pt}/\text{Co}/\text{NiO}/\text{Pt}$ devices, large on/off ratio ($\approx 10^5$) could be obtained at room temperature with distinguished HRS and LRS, which correspond to distinct EB and negligible EB, respectively. The E-field control of EB in combination with RS in AFM/FM heterostructures paves a new way for designing magneto-electric random access memories (MERAMs). It is also promising for future development of multifunctional and nonvolatile memory devices.

Figure 1a schematically illustrates the device's stacking structure and the measurement geometry as well. In order to achieve both significant EB and good RS performance in the present devices, a combined NiO layer, constituted by NiO(1), and NiO(2) layers with low and high oxidation levels, respectively, is employed in the present study. The electric and magnetic results for samples with only NiO(1) layer or NiO(2) layer can be seen in Figure S1, Supporting Information. To characterize the degrees of oxidation of the two NiO layers, the X-ray photoemission spectroscopy (XPS) depth profiling was performed on the as-prepared sample. The XPS spectra were corrected using the maximum of the adventitious C 1s signal at 284.8 eV. It is noted that the XPS experiments were carried out on the sample surface region where the top Pt electrodes have not covered, i.e., the areas between the neighboring Pt electrodes. The XPS spectra were recorded respectively after etching the sample for 300 and 500 s with the etching rate evaluated to be about 0.1 nm s^{-1} . Therefore, the oxidation states of Ni in different NiO layers can be detected. As shown in Figure 1b, the top and bottom XPS panels correspond to NiO(2) and NiO(1) layers, respectively. After careful fitting, all the peaks can be distinguished. One of them for NiO(1) layer shows a metallic nickel ($\text{Ni}^0\text{-}2\text{p}^{3/2}$) peak at the binding energy of 852.4 eV. The other two peaks for both NiO(1) and NiO(2) layer are located at the binding energies of 854.0 and 855.5 eV, which are corresponding to $\text{Ni}^{2+}\text{-}2\text{p}^{3/2}$. Moreover, an obvious peak at 861.4 eV is recognized as the satellite peak for $\text{Ni}^{2+}\text{-}2\text{p}^{3/2}$. The XPS spectra analysis also indicate that the Ni ions with their valences larger than 2 are absent, eliminating the other nickel-oxides, such as Ni_2O_3 , NiO_2 , in the sample. The most striking result is that Ni^0 atoms can be clearly observed in the NiO(1) layer while hardly detectable in the NiO(2) layer, indicating that the NiO(2) layer is almost fully oxidized while the NiO(1) layer still contains metallic Ni atoms besides the NiO compounds.

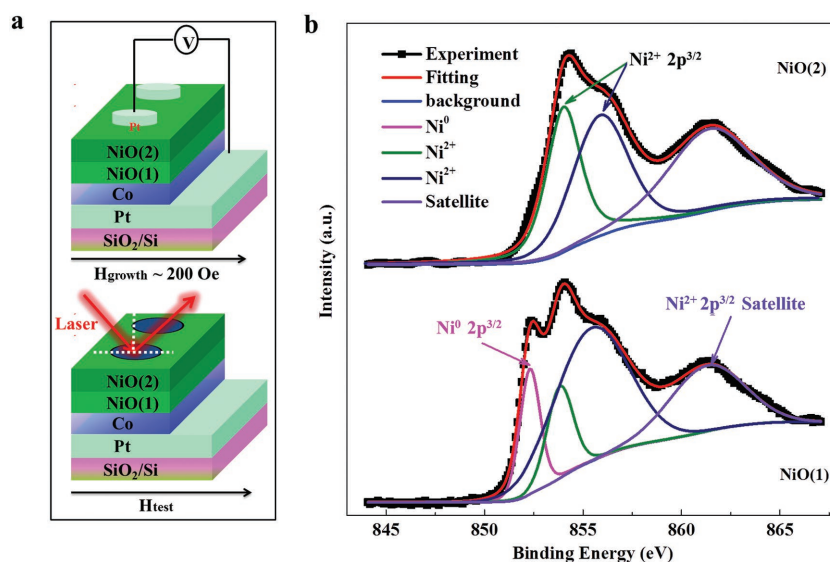


Figure 1. Electric, magneto-optical measurement geometry and XPS spectra. a) Schematic illustration of the stacking structure, I – V measurement (top panel) and focused MOKE measurement after removal of the top Pt electrodes (bottom panel) for the $\text{Si}/\text{SiO}_2/\text{Pt}/\text{Co}/\text{NiO}(1)/\text{NiO}(2)/\text{Pt}$ device. b) XPS spectra for NiO(1) (bottom panel) and NiO(2) (top panel), respectively.

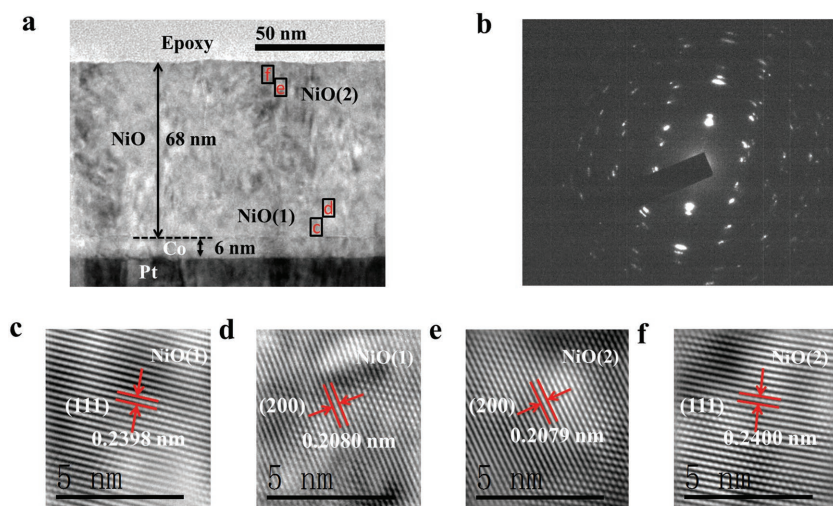


Figure 2. Microstructure characterization by TEM. a,b) The cross-sectional TEM image and SAD pattern of the Pt/Co/NiO multilayer film. c–f) The HRTEM images corresponding to the locations denoted by “c, d, e, f” in (a).

The bright-field cross-sectional transmission electron microscopy (TEM) images of the Pt/Co/NiO multilayer film are shown in **Figure 2**, which exhibit the good stacking structure and sharp interfaces. As shown in Figure 2a, there is no clear interface between NiO(1) and NiO(2) layers, which is possibly due to the reason that they have the same crystalline structure and lattice parameters. The thicknesses of the Co and the NiO

layers are about 6 and 68 nm, respectively, in good agreement with the nominal ones. Moreover, the NiO layer has a columnar structure with the width of the columnar grain of about 15 nm (Figure S2, Supporting Information). Figure 2b shows the selected area electron diffraction (SAED) pattern of the sample, which verifies the polycrystalline structure for the NiO layers. Furthermore, from the high-resolution TEM (HRTEM) images shown in Figure 2c–f with respect to the labeled locations in the NiO layers, the interplanar spacings are measured to be about 0.2400/0.2389 and 0.2080/0.2079 nm, corresponding to NiO (111) and (200) planes, respectively. These results are in good agreement with the X-ray diffraction (XRD) patterns (Figure S3, Supporting Information).

Figure 3 shows a typical unipolar RS behavior in the Si/SiO₂/Pt/Co/NiO/Pt cell. That is, this cell can be switched from HRS to LRS or vice versa without changing the voltage polarity. The current–voltage (*I*–*V*) curves of the cells were studied by dc voltage sweeping, and the results are displayed in both linear (Figure 3a) and semilogarithmic scales (Figure 3b). Within the first sweep starting at 0 V, the Pt/Co/NiO/Pt system displays a sudden current increase at a voltage of about 4.3 V due to the forming process of the cell. The current increase is limited by a current compliance (CC) with its

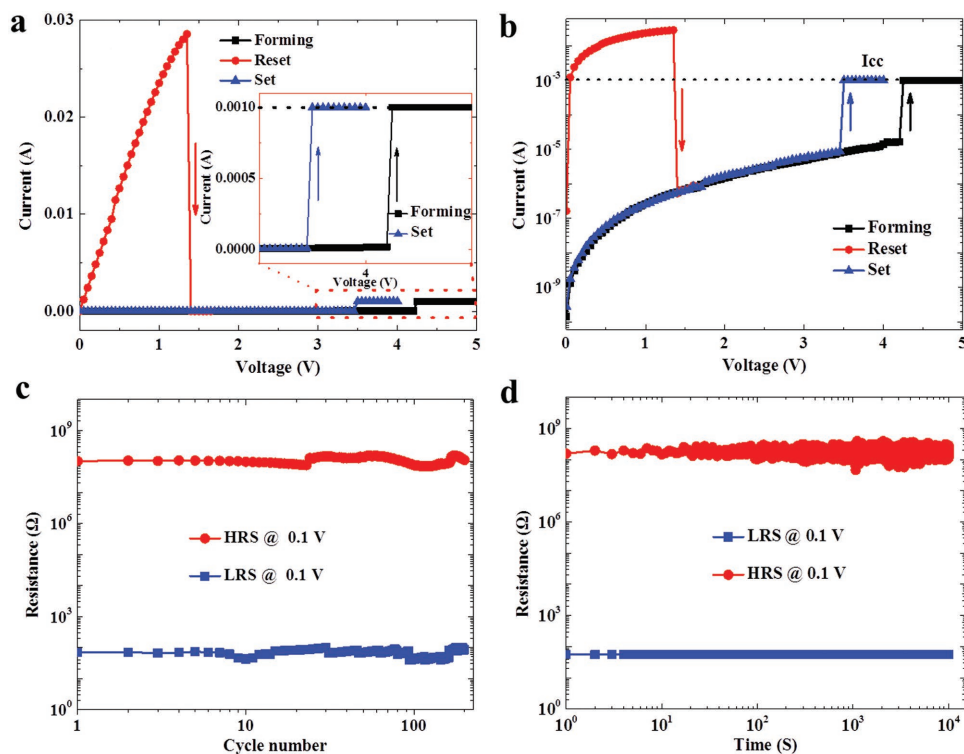


Figure 3. Resistive switching performance characterization. a,b) Typical *I*–*V* curves of the Pt/Co/NiO/Pt devices in both linear scale and semilogarithmic scale. The inset is the zoom-in of the red dashed box region. The arrows indicate the voltage sweeping directions. c,d) The cycle number and retention time dependences of the device’s resistance at HRS and LRS under an applied voltage of 0.1 V.

value (I_{cc}) of 1 mA. After the forming process, the cell turns into the ON state (i.e., LRS). Thereafter, the system can be RESET by releasing the CC and increasing the voltage until the cell abruptly turns into the OFF state (i.e., HRS) at the RESET voltage of about 1.4 V. With increasing the applied voltage from zero again, the cell turns back into the ON state when the voltage was above the “SET” value of about 3.5 V, which is obviously lower than the forming voltage. Afterward, the entire cycle changing between HRS and LRS can be repeated. These I - V curves describing the RS behavior are in good agreement with the previous reports of Pt/NiO/Pt system.^[22] We also investigated the reliability and stability of the two-state RS characteristic of the cell. Figure 3c shows the cycle number dependence of the cell's resistance at LRS and HRS, respectively. Although the 200 cycles shown in the endurance test in Figure 3c are encouraging, practical devices will require thousands or millions of switching cycles. As shown in Figure 3d, the resistances at both LRS and HRS keep almost unchanged under a fixed applied voltage of 0.1 V even after 10^4 s, which demonstrates a good retention time performance for the cell. Moreover, the on/off ratio (R_{HRS}/R_{LRS}) is larger than 10^5 (see Figure 3c,d), allowing one to distinguish the two resistance states easily in a real working device. The mechanism responsible for the above RS behavior will be addressed in the latter parts. To further understand the RS behavior, several conduction models have been used to fit the I - V data (Figure S4, Supporting Information). The fitting results demonstrate that the Ohmic conduction and space charge limited conduction (SCLC) mechanisms are responsible for the LRS and HRS, respectively.

Figure 4 shows the typical M - H loops for different cells on the sample measured by focused magneto-optic Kerr effect

(FMOKE) magnetometer. Before the M - H loop measurements, the cells were set at different resistance states by applying certain voltages and all the top Pt electrodes were removed by ion beam etching (IBE). In Figure 4a, the red circles represent the laser spot probing areas and the letters of “O,” “L,” and “H” indicate that the probing cell is at original state (O-S, without applying any voltages), LRS state and HRS, respectively. Moreover, the red circle with a letter of “Q” in the middle denotes the probing area overlapping LRS and O-S. As shown in Figure 4b, clear left shift of the M - H loop along the magnetic field axis can be observed, confirming the establishment of EB in the original state (O-S). The quantities of the EB field and coercivity are defined as $H_E = -(H_{CL} + H_{CR})/2$ and $H_C = (H_{CR} - H_{CL})/2$, respectively. Here H_{CL} and H_{CR} are the coercive fields for the descending and ascending branches of the M - H loop, respectively. Then, H_E is determined to be 20 Oe for O-S. The inset of Figure 4b exhibits the M - H loop of a 6 nm Co film without neighboring NiO layers, which shows that H_E is zero and H_C is about 16 Oe. As shown in Figure 4c, the M - H loops indicate that H_E is about 19.1 Oe for HRS, which is almost the same as that for O-S, and nearly zero for LRS. Moreover, H_C is calculated to be about 23 Oe for LRS, which is obviously larger than that (16 Oe) of a single Co layer with the same thickness, suggesting that weak interfacial coupling still exists between the Co and NiO layers for LRS. Comparing the M - H loop for HRS with that for LRS, one can find that the descending branch moves rightward significantly, whereas the ascending branch keeps almost unchanged. Therefore, when the laser spot is located at the “Q” region which spans over LRS and O-S, the resultant M - H loop will be the superposition of the O-S- and LRS-loops, which is verified in Figure 4d. As shown in

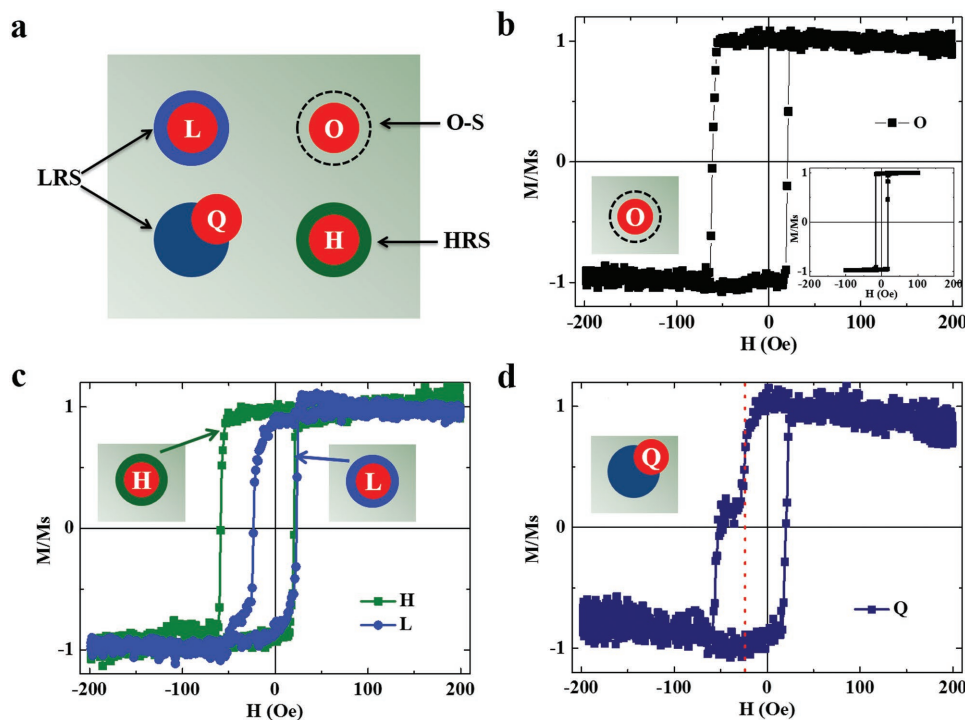


Figure 4. Electric field control of exchange bias. a) Schematic illustration for different laser spot detection locations on the sample. (b), (c), and (d) show the M - H loops where the device is in O-S, HRS/LRS, and Q, respectively. The inset displays the M - H loop of a Pt(50 nm)/Co(6 nm)/Pt(50 nm) film.

the inset of Figure 4d, because the laser spot covers about 50% LRS and 50% O-S region, the O-S- and LRS-loops seem to be comparable. However, when the laser spot is deviated from this position, the superposed $M-H$ loop will change significantly with different proportions of the two loops (Figure S5, Supporting Information). Moreover, it needs to be emphasized that we have measured a lot of cells preset at different resistance states (HRS or LRS) and the above similar EB results could be obtained (Figure S6, Supporting Information).

The RS behavior and the correlation between RS and EB in the present system can be understood based on the conductive filamentary model.^[16,23] It is well accepted that NiO is a p-type wide-bandgap semiconductor, where the major injected carriers are holes.^[24,25] The Joule heating effect, which facilitates the redox reaction, is most serious near the anodic interface where hole injection occurs. When oxygen ions are lost by the redox reaction at the anodic interface, Ni interstitials (Ni_i'') can be formed through the following reaction^[26]



Therefore, the Ni_i'' ions generated at the anodic interface initially may drift/diffuse toward the cathode interface and meet together to form tiny metallic Ni filaments when their quantities become large enough. Finally, the conductive filaments (CFs) are produced by the percolated metallic Ni chains in the form of dendrite-like or random network.^[26] After such a “Forming” or “SET” process, the device turns into LRS.

As shown in the top panel of Figure 5a, the NiO layer at O-S contains some nanometer-sized conductive domains at highly localized areas, such as the grain boundaries (dash lines).^[23] Furthermore, first-principles calculation suggests low migration energy at the grain boundary.^[27] Therefore, one may con-

sider that Ni atoms move along the grain boundaries to form CFs in the beginning of the “Forming” or “SET” process, as exhibited by the blue vertical lines in the top panel of Figure 5b,c. However, when the CFs grow toward the cathode, they may pass through the original grain boundaries or the non-grain boundary regions (blue nonvertical lines). Similar results can be also found in previous reports.^[28,29] When the device is at O-S, due to interfacial exchange coupling between Co and NiO, EB will be established easily. After the device is positively biased and transformed from O-S to LRS, multiple Ni CFs may be formed throughout the entire NiO layer^[29,30] and reach the NiO–Co interface, which will possibly damage the AFM structure there, leading to reduced or even disappeared EB. The relevant magnetic moment arrangements of the Ni and Co atoms around the NiO–Co interface in different resistance states are illustrated in the bottom panels of Figure 5a–c. In order to further demonstrate the reduced EB by introducing Ni CFs into the NiO layer, we performed the relevant Monte Carlo simulation (Figure S7, Supporting Information). The simulation results clearly show that the EB field decreases quickly in the beginning and then approaches zero with increasing p , i.e., the fraction of Ni CFs. Moreover, the simulated $M-H$ loops illustrate that the coercive field at the descending branch decreases quickly in the initial stage and then slowly with increasing p , while at the ascending branch it is roughly independent of p . These calculation results are in good agreement with the experimental findings, suggesting that the generation of multiple Ni CFs throughout the NiO layer is reasonable to account for the experimental EB phenomena.

For the unipolar RS behavior in NiO, although some studies revealed evidence for one or few CFs in a much localized region by TEM,^[16,29,30] there have been some reports implying that multi-nanofilaments are formed at LRS in a cell device.^[28,29,31,32] In the present study, from the cross-sectional HRTEM images

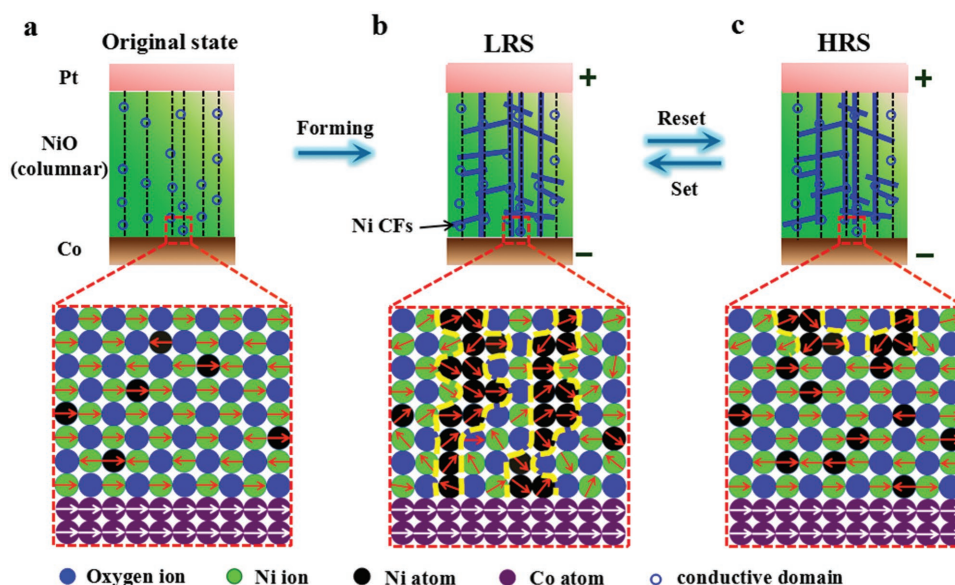


Figure 5. The mechanism responsible for the correlation between resistive switching and exchange bias. a–c) Top three panels schematically illustrate the “Forming,” “SET,” and “RESET” processes when the positively biased Pt/Co/NiO/Pt device is in O-S, LRS, and HRS, respectively. Bottom three panels exhibit the corresponding magnetic moment arrangements of the Ni and Co atoms around the NiO–Co interface when the device is in O-S a), LRS b), and HRS c), respectively. Moreover, the yellow lines in (b) and (c) denote the basic outlines of the Ni conductive filaments.

(Figure S8, Supporting Information) obtained on a single cell at LRS, the tree-branch-like nanofilaments can be easily observed in different regions near the NiO–Co interface, indicating multiple nanofilaments generated in a cell. However, due to irregular shape and 3D in nature for the nanofilaments, it is very hard to figure out the density of the nanofilaments by TEM directly. Apart from the multiple CFs mechanism, one may argue that oxidation and reduction under electric fields may occur at the Co–NiO interface, resulting in Co/CoO/NiO and Co/NiO, respectively, which may also explain the EB phenomena. Although this kind of magneto-ionic control of EB has been found in some systems very recently^[33] by using electric field to reversibly control the interface magnetism,^[34–36] this mechanism could be easily excluded in the present study. First, the XPS depth profile of “Co 2p” (Figure S9, Supporting Information) indicates that CoO can be hardly detectable in the cell before and after the RS process. Second, no obvious change for the *M–H* loop can be observed after the cell was positively or negatively biased (Figure S9, Supporting Information), implying that O^{2–} ions are unlikely to migrate under electric fields and thus oxidation and reduction of Co can hardly happen under the voltage less than the forming voltage.

Finally, after a “RESET” process, the device will enter HRS because the CFs has been ruptured. As mentioned above, the filament grows from the anode interface to the cathode interface. Therefore, the weakest part of the filament is most possibly formed near the cathode, where the rupture and recovery of the filament occur.^[37] However, so far it has still been controversial whether the rupture and connection of Ni filaments take place at the anodic site of the filaments,^[38] the cathode site of the filaments,^[37] or in the bulk of the filaments.^[22,39] In the present study, no obvious change of EB could be observed when the device was at HRS or LRS in comparison with O–S after negative electric-field was applied, which supports the rupture/connection of Ni filaments occurring at the cathode site in our samples. The most likely way of rupture is to move some of the O^{2–} ions from the NiO region nearby the Ni filament to the Ni filament portion near the cathode.^[37] In other words, the Ni filament near the Co–NiO interface will be oxidized to NiO again during the rupture process. Therefore, as shown in Figure 5c, the AFM structure near the Co–NiO interface has been almost recovered after the “RESET” step, leading to the appearance of EB again as that in O–S. Since the RS behavior, i.e., the switching between “SET” and “RESET” processes, is reversible, the E-field control of EB is also reversible. Moreover, since NiO has a relatively high Néel temperature of about 525 K,^[40] the present E-field control of EB by virtue of RS can be operated very stably at room temperature or even higher ones.

In summary, the Si/SiO₂/Pt/Co/NiO/Pt devices have been fabricated by magnetron sputtering, in which both unipolar RS behavior and EB effect can be well controlled by electric field at room temperature. By applying certain voltages, the device can be intentionally set at HRS/LRS with obvious/negligible EB. Considering that the CFs are formed throughout the entire NiO layer and ruptured near the Co–NiO interface under suitable positive voltages, all the correlated RS and EB phenomena can be well explained. This work provides a new approach to achieve reversible E-field controlled EB at room temperature, which could pave a new way to realize multifunctional

and nonvolatile MERAM devices with extremely low energy consumption.

Experimental Section

Device Fabrication: A schematic illustration of the device's stacking structure is shown in Figure 1a. The Pt/Co/NiO/Pt multilayer films were deposited by magnetron sputtering at room temperature on Si (100) substrate with native oxide on the surface. Before the film deposition, the commercial Si wafers were diced into about 1 cm × 1 cm pieces as substrates and cleaned by proper procedures. The sputtering targets of Pt, Co, and NiO were purchased commercially and their purities are all larger than 99.99%. The base pressure was lower than 5.0 × 10^{–6} Pa and the Ar pressure was kept at 0.3 Pa during the deposition for all the metal films. A Pt film of about 50 nm was first deposited on the substrate as the bottom electrode, followed by a 6 nm Co layer made by dc sputtering. Afterward, the first NiO layer (i.e., NiO(1), *t*₁ ≈ 20 nm) was deposited by rf sputtering with pure Argon gas. In order to increase the insulation level of the film, the second NiO layer (i.e., NiO(2), *t*₂ ≈ 50 nm) was made by reactive rf sputtering with mixed gases of Argon and Oxygen (*P*_{Ar}: *P*_{O₂} = 5: 2). During deposition of the NiO layers, the sputtering power and the working gas pressure were maintained at 80 W and 0.5 Pa, respectively. Finally, for making the top electrode, another Pt layer of about 50 nm was deposited on the top NiO layer using shadow mask and the diameter of the top electrode is about 250 μm. Note that all the thicknesses mentioned above are nominal. To establish EB of the Co/NiO bilayer, a constant magnetic field of about 200 Oe was applied parallel to the film plane during the film deposition and no further field cooling was carried out.

Characterizations: The RS behavior of the sample was characterized by a Keithley-2400 meter with the wires' connection illustrated in the top panel of Figure 1a. Note that the positive bias is applied with the current flowing from the top Pt electrode to the NiO/Co layer and then to the bottom Pt electrode and the negative bias is applied with the current flowing in the opposite direction. The in-plane magnetic hysteresis (*M–H*) loops were measured by a commercial FMOKE (NanoMOKE 3) magnetometer with the magnetic field applied in the film plane and parallel to the incident plane of light as well, as shown in the bottom panel of Figure 1a. The FMOKE system utilized a 660 nm red laser light with a spot size of about 200 μm. In order to let the probe light reach the Co layer to accomplish the FMOKE measurement, the top Pt electrodes were removed by IBE prior to the measurements. XPS (Thermo-scientific K-Alpha) measurements were carried out in an ultrahigh vacuum system using Al Kα radiation as the X-ray source. The microstructure of sample was also characterized by a JEOL 2200FS TEM equipped with an Omega filter for energy-filtered imaging, working at 200 kV accelerating voltage. The site-specific specimen preparation for TEM observation was prepared based on a typical lift-out technique in a ZEISS Auriga scanning electron microscopy/focus ion beam (SEM/FIB), as shown in Figure S10, Supporting Information. All the measurements and characterizations were performed at room temperature.

Supporting Information

Supporting Information is available from the Wiley Online Library or from the author.

Acknowledgements

This work was supported by National Basic Research Program of China (No. 2014CB921101), National Key Research and Development Program of China (No. 2016YFA0300803), National Natural Science Foundations of China (Nos. 51471085, 51331004, 51771053, 11174131, and 61274102), and Australian Research Council (No. DP150100018).

Conflict of Interest

The authors declare no conflict of interest.

Keywords

conductive filaments, electric control, exchange bias, resistive switching

Received: March 24, 2018

Revised: April 30, 2018

Published online: June 11, 2018

- [1] S. Wolf, D. Awschalom, R. Buhrman, J. Daughton, S. Von Molnar, M. Roukes, A. Y. Chtchelkanova, D. Treger, *Science* **2001**, 294, 1488.
- [2] I. Zutic, J. Fabian, S. Das Sarma, *Rev. Mod. Phys.* **2004**, 76, 323.
- [3] X. He, Y. Wang, N. Wu, A. N. Caruso, E. Vescovo, K. D. Belashchenko, P. A. Dowben, C. Binek, *Nat. Mater.* **2010**, 9, 579.
- [4] C. Song, B. Cui, F. Li, X. Zhou, F. Pan, *Prog. Mater. Sci.* **2017**, 87, 33.
- [5] W. H. Meiklejohn, C. P. Bean, *Phys. Rev.* **1956**, 102, 1413.
- [6] J. Nogués, I. K. Schuller, *J. Magn. Magn. Mater.* **1999**, 192, 203.
- [7] C. Chappert, A. Fert, F. N. Van Dau, *Nat. Mater.* **2007**, 6, 813.
- [8] X. Chen, A. Hochstrat, P. Borisov, W. Kleemann, *Appl. Phys. Lett.* **2006**, 89, 202508.
- [9] P. Borisov, A. Hochstrat, X. Chen, W. Kleemann, C. Binek, *Phys. Rev. Lett.* **2005**, 94, 117203.
- [10] V. Laukhin, V. Skumryev, X. Marti, D. Hrabovsky, F. Sanchez, M. V. Garcia-Cuenca, C. Ferrater, M. Varela, U. Luders, J. F. Bobo, J. Fontcuberta, *Phys. Rev. Lett.* **2006**, 97, 227201.
- [11] S. M. Wu, S. A. Cybart, P. Yu, M. D. Rossell, J. X. Zhang, R. Ramesh, R. C. Dynes, *Nat. Mater.* **2010**, 9, 756.
- [12] S. M. Wu, S. A. Cybart, D. Yi, J. M. Parker, R. Ramesh, R. C. Dynes, *Phys. Rev. Lett.* **2013**, 110, 067202.
- [13] J. T. Heron, M. Trassin, K. Ashraf, M. Gajek, Q. He, S. Y. Yang, D. E. Nikonov, Y. H. Chu, S. Salahuddin, R. Ramesh, *Phys. Rev. Lett.* **2011**, 107, 217202.
- [14] M. Liu, J. Lou, S. Li, N. X. Sun, *Adv. Funct. Mater.* **2011**, 21, 2593.
- [15] A. Chen, Y. Zhao, P. Li, X. Zhang, R. Peng, H. Huang, L. Zou, X. Zheng, S. Zhang, P. Miao, Y. Lu, J. Cai, C. W. Nan, *Adv. Mater.* **2016**, 28, 363.
- [16] M. J. Lee, S. Han, S. H. Jeon, B. H. Park, B. S. Kang, S. E. Ahn, K. H. Kim, C. B. Lee, C. J. Kim, I.-K. Yoo, *Nano Lett.* **2009**, 9, 1476.
- [17] D. H. Kwon, K. M. Kim, J. H. Jang, J. M. Jeon, M. H. Lee, G. H. Kim, X. S. Li, G. S. Park, B. Lee, S. Han, M. Kim, C. S. Hwang, *Nat. Nanotechnol.* **2010**, 5, 148.
- [18] J. Y. Chen, C. L. Hsin, C. W. Huang, C. H. Chiu, Y. T. Huang, S. J. Lin, W. W. Wu, L. J. Chen, *Nano Lett.* **2013**, 13, 3671.
- [19] Y. Yang, P. Gao, L. Li, X. Pan, S. Tappertzhofen, S. Choi, R. Waser, I. Valov, W. D. Lu, *Nat. Commun.* **2014**, 5, 4232.
- [20] S. Cho, C. Yun, S. Tappertzhofen, A. Kursumovic, S. Lee, P. Lu, Q. Jia, M. Fan, J. Jian, H. Wang, S. Hofmann, J. L. MacManus-Driscoll, *Nat. Commun.* **2016**, 7, 12373.
- [21] D. S. Jeong, R. Thomas, R. S. Katiyar, J. F. Scott, H. Kohlstedt, A. Petraru, C. S. Hwang, *Rep. Prog. Phys.* **2012**, 75, 076502.
- [22] I. Daniele, R. Bruchhaus, R. Waser, *Phase Transitions* **2011**, 84, 570, and references therein.
- [23] G. S. Park, X. S. Li, D. C. Kim, R. J. Jung, M. J. Lee, S. Seo, *Appl. Phys. Lett.* **2007**, 91, 222103.
- [24] S. Park, H. S. Ahn, C. K. Lee, H. Kim, H. Jin, H. S. Lee, S. Seo, J. Yu, S. Han, *Phys. Rev. B* **2008**, 77, 134103.
- [25] P. Lunkenheimer, A. Loidl, C. R. Ottermann, K. Bange, *Phys. Rev. B* **1991**, 44, 5927.
- [26] K. M. Kim, D. S. Jeong, C. S. Hwang, *Nanotechnology* **2011**, 22, 254002.
- [27] C. Park, S. H. Jeon, S. C. Chae, S. Han, B. H. Park, S. Seo, D. W. Kim, *Appl. Phys. Lett.* **2008**, 93, 042102.
- [28] J. Y. Son, Y. H. Shin, *Appl. Phys. Lett.* **2008**, 92, 222106.
- [29] Y. In Kyeong, K. Bo Soo, A. Seung Eon, L. Chang Bum, L. Myoung Jae, P. Gyeong-Su, L. Xiang-Shu, *IEEE Trans. Nanotechnol.* **2010**, 9, 131.
- [30] Y. Luo, D. Zhao, Y. Zhao, F. Chiang, P. Chen, M. Guo, N. Luo, X. Jiang, P. Miao, Y. Sun, A. Chen, Z. Lin, J. Li, W. Duan, J. Cai, Y. Wang, *Nanoscale* **2015**, 7, 642.
- [31] Y. Q. Xiong, W. P. Zhou, Q. Li, M. C. He, J. Du, Q. Q. Cao, D. H. Wang, Y. W. Du, *Appl. Phys. Lett.* **2014**, 105, 032410.
- [32] J. Y. Son, C. H. Kim, J. H. Cho, Y. H. Shin, H. M. Jang, *ACS Nano* **2010**, 4, 3288.
- [33] D. A. Gilbert, J. Olamit, R. K. Dumas, B. J. Kirby, A. J. Grutter, B. B. Maranville, E. Arenholz, J. A. Borchers, K. Liu, *Nat. Commun.* **2016**, 7, 11050.
- [34] C. Bi, Y. Liu, T. Newhouse-Illige, M. Xu, M. Rosales, J. W. Freeland, O. Mryasov, S. Zhang, S. G. E. te Velthuis, W. G. Wang, *Phys. Rev. Lett.* **2014**, 113, 267202.
- [35] U. Bauer, L. Yao, A. J. Tan, P. Agrawal, S. Emori, H. L. Tuller, S. van Dijken, G. S. D. Beach, *Nat. Mater.* **2015**, 14, 174.
- [36] D. A. Gilbert, A. J. Grutter, E. Arenholz, K. Liu, B. J. Kirby, J. A. Borchers, B. B. Maranville, *Nat. Commun.* **2016**, 7, 12264.
- [37] K. M. Kim, B. J. Choi, S. J. Song, G. H. Kim, C. S. Hwang, *J. Electrochem. Soc.* **2009**, 156, G213.
- [38] K. Kinoshita, T. Tamura, M. Aoki, Y. Sugiyama, H. Tanaka, *Appl. Phys. Lett.* **2006**, 89, 103509.
- [39] D. Y. Zhao, S. Qiao, Y. X. Luo, A. T. Chen, P. F. Zhang, P. Zheng, Z. Sun, M. H. Guo, F. Chiang, J. Wu, J. L. Luo, J. Q. Li, S. Kokado, Y. Y. Wang, Y. G. Zhao, *ACS Appl. Mater. Interfaces* **2017**, 9, 10835.
- [40] A. Berkowitz, K. Takano, *J. Magn. Magn. Mater.* **1999**, 200, 552.